LiDAR Data Association Risk Reduction Using Tight Integration with INS

Ali Hassani and Mathieu Joerger, The University of Arizona,
Guillermo Duenas Arana and Matthew Spenko, Illinois Institute of Technology

Abstract

This paper describes the design and analysis of a new method to integrate measurements from light detection and ranging (LiDAR) and inertial navigation systems (INS). The tight integration scheme aims at facilitating safety risk evaluation while exploiting complementary properties of LiDAR and INS. In particular, INS is used to improve LiDAR prediction of position and orientation (or pose), thereby reducing the risk of incorrectly associating scanned features with mapped landmarks. Moreover, LiDAR pose estimation updates can limit the drift of INS errors over time.

1. Introduction

This work aims at quantifying safety risks in navigation systems using light detection and ranging (LiDAR – or laser scanner) and inertial navigation systems (INS) for automated vehicle applications. Navigation safety is measured in terms of 'integrity', a performance measure used in civilian aviation. Integrity is a measure of trust in sensor information. Integrity requirements can be set independently of navigation system and vehicle design.

Over the past 30 years, several integrity risk evaluation methods have been developed in Global Navigation Satellite System (GNSS)-based aviation applications to ensure the safety of passengers and pilots [1, 2]. However, the same methods do not directly apply to highly automated vehicles (HAV) because GNSS signals cannot be reliably tracked on the ground. Buildings and trees can alter or block satellite signals.

Other types of sensors such as LiDARs, radars or cameras are needed for HAV navigation. This work focuses on LiDARs because of their prevalence in HAVs. Each individual LiDAR data-point carries little useful navigation information. Raw LiDAR data must be pre-processed before being sent to a 'pose' estimator (pose stands for position and orientation). Two pre-estimator procedures can be conducted: feature extraction (FE) and data association (DA). The purpose of FE is to find consistently recognizable and viewpoint-invariant landmarks. Landmark features should be detectable and distinguishable in successive scans. DA assigns these extracted features to assumed landmarks in the estimation process. Finding the correct ordering between extracted features and stored (or mapped) landmarks is essential: incorrect associations can result in navigation errors that can compromise system integrity [3, 4]. FE and DA can be challenging in the presence of sensor uncertainty. This is why many sophisticated algorithms have been devised [5-8]. But, these do not assess the risk of incorrect association.

Relevant approaches in multi-target tracking describe methods to evaluate the probability of correct association in the presence of measurement uncertainty [6, 9-11]. However, these algorithms are not well suited for safety-critical HAV applications due to their lack of prediction capability, to approximations that do not necessarily upper-bound risks, and to high computational loads. Also, the risk of FE is not addressed. Overall, research on integrity and continuity of FE and DA is sparse.

This paper builds upon prior work in [12-14], where we developed an analytical integrity risk prediction method for FE and DA. At the FE step, we established a probabilistic normalized separation metric between landmarks ensuring that they could be reliably and quantifiably distinguished from each other. The ability to distinguish landmarks is instrumental to prevent incorrect associations. We then derived a multiple-hypothesis EKF innovation-based DA process. The EKF innovation-based DA method in [12-14] provides the means to evaluate the probability of incorrect associations while considering all potential measurement permutations (i.e., all potential incorrect associations). This method was used to establish an analytical bound on the integrity risk of laser-based pose estimation over successive iterations. In addition, references [12, 13] showed that the probability of incorrect association could quickly grow in the presence of poorly distinguishable landmarks. One approach to mitigate this problem is to select a subset of features sensed by the LiDAR in

the environment [14, 15]. But, subset selection reduces the number of redundant associations, and reduces the ability to detect unwanted, unmapped landmarks in view of the LiDAR [14].

As an alternative to landmark selection, integration of LiDAR with INS can help improve pose prediction, and hence increase the success rate of EKF innovation-based data associations. Prior work on LiDAR/INS integration includes loose and tight coupling schemes primarily aimed at using INS to coast between LiDAR pose updates and at using LIDAR updates to calibrate INS biases [16]. One implementation also uses the INS to determine the laser scanner's tilt angle [17, 18]. In this implementation, the INS calibration is performed in the laser's extracted feature measurement domain rather than in the pose domain. To our knowledge, risk evaluation for LiDAR/INS is not addressed in the literature.

In response, in this paper, we develop a tightly-integrated LiDAR/INS pose estimation process, which is designed to enable integrity risk quantification while reducing the risk of incorrect association.

The first part of the paper describes the tightly-integrated LiDAR/INS method. Non-linear continuous-time process and measurement equations are derived, linearized, and discretized The second part of the paper provides an overview of the multiple-hypothesis DA risk evaluation method [10]. The focus of the description is on the contribution of INS measurements for the innovation-based nearest-neighbor association criterion. In a third part of the paper, we present simulation results and analyses. A covariance analysis is carried out for an example scenario of a vehicle equipped with a LiDAR/INS system driving by two landmarks.

2. INS/ LiDAR Tight Coupling

2.1 INS Measurement model

In this section, continuous-time equations are derived for a strapdown INS fixed to an HAV following the same steps as in [19, 20]. The discrete-time equations are given in Appendix A.

2.1.1 Nonlinear HAV Acceleration Equation

The first step in modeling INS measurements is to define HAV trajectory state parameters and reference coordinate frames. INS accelerometers measure vehicle acceleration with respect to the inertial frame (labeled 'I') and HAV position and orientation must be expressed in the navigation frame 'N' (for example, in the East, North, Up directions). HAV motion is described relative to the earth frame 'E', which is earth-centered, earth-fixed. In addition, the INS is fixed in the HAV body frame 'B', which can be oriented along the vehicle's maximum moment of inertia axes as described in [17, 18].

We use the Newton and Euler method to describe the translational and rotational motion of the HAV. The vehicle's velocity with respect to earth frame 'E' differentiated with respect to navigation frame 'N' (derivative of ground velocity with respect to navigation frame) is expressed as [19]:

$$^{N}\dot{\mathbf{v}}_{HAV}^{E}(t) = {}^{N}\mathbf{f}^{I}(t) - (2\,{}^{N}\boldsymbol{\omega}^{IE}(t) + {}^{N}\boldsymbol{\omega}^{EN}(t)) \times {}^{N}\mathbf{v}_{HAV}^{E}(t) + {}^{N}\mathbf{g}^{E}(t) \tag{1}$$

where

t is time (to indicate continuous-time variables in contrast with discrete-time expressions later in the derivation)

$^{N}\dot{\mathbf{v}}_{HAV}^{E}$ is the 3×1 derivative of ground speed with respect to (w.r.t.) navigation frame

$^{N}\mathbf{v}_{HAV}^{E}$ is the 3×1 vehicle velocity with respect to earth, and expressed in the navigation frame

$^{N}\mathbf{f}^{I}$ is the 3×1 specific force vector at point P w.r.t. frame I expressed in N [19]

$^{N}\boldsymbol{\omega}^{IE}$ is the angular velocity vector of frame E w.r.t frame I expressed in N

$^{N}\boldsymbol{\omega}^{EN}$ is the angular velocity vector of frame N w.r.t frame E expressed in N

$^{N}\mathbf{g}^{E}$ is the local gravity vector at point P w.r.t frame E expressed in N [19, 20].

2.1.2   INS Sensor Error Model

An INS provides measures of the specific force $^{B}\mathbf{f}^{I}$ and of the angular velocity vector of the sensor's body frame 'B' with respect to I $^{B}\boldsymbol{\omega}^{IB}$ both expressed in frame B. The following equations are used to model the continuous-time form of the errors impacting the INS specific force measurement. Discrete-time forms of these equations can be found in Appendix A [20].

$$^{B}\tilde{\mathbf{f}}^{I}(t)=[\mathbf{I}+\mathbf{S}_{a,\,SF}+\mathbf{M}_{a,\,MIS}]\,^{B}\mathbf{f}^{I}(t)+\mathbf{b}_{a0}+\mathbf{b}_{a}(t)+\boldsymbol{\upsilon}_{a}(t) \tag{2}$$

$$^{B}\overline{\mathbf{f}}^{I}(t)=[\mathbf{I}+\hat{\mathbf{S}}_{a,\,SF}+\hat{\mathbf{M}}_{a,\,MIS}]^{-1}(^{B}\tilde{\mathbf{f}}^{I}(t)-\hat{\mathbf{b}}_{a0}) \tag{3}$$

where
$^{B}\mathbf{f}^{I}(t)$ is the 3×1 true specific force vector expressed in body frame B

$^{B}\tilde{\mathbf{f}}^{I}(t)$ is the measured specific force vector expressed in B

$\mathbf{S}_{a,\,SF}$ and $\mathbf{M}_{a,\,MIS}$ are the actual accelerometer scale factor and misalignment matrices in B

$\hat{\mathbf{S}}_{a,\,SF}$ and $\hat{\mathbf{M}}_{a,\,MIS}$ are the estimated accelerometer scale factor and misalignment matrices in B

$\mathbf{b}_{a0}$ is the actual accelerometer constant bias vector in B

$\hat{\mathbf{b}}_{a0}$ is the accelerometer bias vector in B estimated using manufacturer specifications

$\mathbf{b}_{a}(t)$ is the accelerometer time-varying bias vector in B

$\boldsymbol{\upsilon}_{a}(t)$ is accelerometer measurement's white noise error component expressed in B

$^{B}\overline{\mathbf{f}}^{I}(t)$ is the estimated specific force vector in B after correcting $^{B}\tilde{\mathbf{f}}^{I}(t)$ using known parameters $\hat{\mathbf{b}}_{a0}$, $\hat{\mathbf{S}}_{a,\,SF}$ and $\hat{\mathbf{M}}_{a,\,MIS}$

In equation (2), $^{B}\mathbf{f}^{I}(t)$ is the true value of the specific force which is not known. The INS measures the specific force, and this raw measurement is noted $^{B}\tilde{\mathbf{f}}^{I}(t)$. Equation (2) expresses the fact that the accelerometer scale factor and misalignment matrices affect the measured specific force. Manufacturers usually provide estimates of these parameters. Scale factor and misalignment errors are corrected in $^{B}\overline{\mathbf{f}}^{I}(t)$, which is the vector used in practice as accelerometer output.

The time-varying part of the accelerometer bias $\mathbf{b}_{a}(t)$ can be modeled as a first order Gauss Markov Random Process (GMRP) [19, 21], and the continuous-time can be written as:

$$\dot{\mathbf{b}}_{a}(t)=-\frac{1}{\tau_{a}}\mathbf{b}_{a}(t)+\mathbf{n}_{a}(t) \tag{4}$$

where
τ_{a} is the GMRP time constant

$\mathbf{n}_{a}$ is the GMRP driving white noise

The discrete-time forms of equations (2) to (4) are provided in Appendix A. In equations (2) to (4), subscript 'a' stands for accelerometer. We can write the same equations for the angular velocity vector of the body frame with respect to the inertial frame $^{B}\boldsymbol{\omega}^{IB}$ which is measured by gyroscopes.

$$^{B}\tilde{\boldsymbol{\omega}}^{IB}(t)=[\mathbf{I}+\mathbf{S}_{g,\,SF}+\mathbf{M}_{g,\,MIS}]\,^{B}\boldsymbol{\omega}^{IB}(t)+\mathbf{b}_{g0}+\mathbf{b}_{g}(t)+\boldsymbol{\upsilon}_{g}(t) \tag{5}$$

$$^{B}\overline{\boldsymbol{\omega}}^{IB}(t)=[\mathbf{I}+\hat{\mathbf{S}}_{g,\,SF}+\hat{\mathbf{M}}_{g,\,MIS}]^{-1}(^{B}\tilde{\boldsymbol{\omega}}^{IB}(t)-\hat{\mathbf{b}}_{g0}) \tag{6}$$

$$\dot{\mathbf{b}}_{g}(t)=-\frac{1}{\tau_{g}}\mathbf{b}_{g}(t)+\mathbf{n}_{g}(t) \tag{7}$$

2.1.3 Linearized INS Equations

The INS equation's state parameters include HAV position, velocity, orientation, and INS biases. The continuous-time state propagation model is linearized using a first order Taylor series expansion about reference state parameter values [3]. We use the notation ' δ ' to indicate deviations of state parameters relative to the reference values. Using INS measurement error equations (3) and (6) and accelerometer and gyro bias equations (4) and (7), we can write a continuous-time linearized state propagation model as:

$$\delta \dot{\mathbf{x}}_{INS} = \mathbf{F}_{INS} \delta \mathbf{x}_{INS} + \delta \mathbf{w}_{INS} \tag{8}$$

$$\delta \mathbf{x}_{INS} = [\delta \mathbf{x}_{HAV}^T \quad \delta \mathbf{v}_{HAV}^T \quad \delta \mathbf{e}_{HAV}^T \quad \delta \mathbf{b}_g^T \quad \delta \mathbf{b}_a^T] \tag{9}$$

$$\mathbf{F}_{INS} = \begin{bmatrix} \mathbf{0} & \mathbf{I} & \mathbf{0} & \mathbf{0} & \mathbf{0} \\ \mathbf{F}_{H2V} & \mathbf{0} & [^N \overline{\mathbf{f}}^I \times] & \mathbf{0} & -\mathbf{C}_B^N \\ \mathbf{0} & \mathbf{F}_{V2T} & -[^N \boldsymbol{\omega}^{IN} \times] & \mathbf{C}_B^N & \mathbf{0} \\ \mathbf{0} & \mathbf{0} & \mathbf{0} & -\tau_g^{-1} \mathbf{I} & \mathbf{0} \\ \mathbf{0} & \mathbf{0} & \mathbf{0} & \mathbf{0} & -\tau_a^{-1} \mathbf{I} \end{bmatrix}, \quad \delta \mathbf{w}_{INS} = \begin{bmatrix} \mathbf{0} \\ \mathbf{C}_B^N (-\delta \mathbf{S}_{a,SF} {}^B \overline{\mathbf{f}}^I - \delta \mathbf{M}_{a,MIS} {}^B \overline{\mathbf{f}}^I - \boldsymbol{\upsilon}_a) \\ -\mathbf{C}_B^N (-\delta \mathbf{S}_{g,SF} {}^B \overline{\boldsymbol{\omega}}^{IB} - \delta \mathbf{M}_{g,MIS} {}^B \overline{\boldsymbol{\omega}}^{IB} - \boldsymbol{\upsilon}_g) \\ \overline{\mathbf{n}}_g \\ \overline{\mathbf{n}}_a \end{bmatrix} \tag{10}$$

where

$\mathbf{C}_B^N$ is the transformation matrix from body to navigation frame [19],

$\mathbf{F}_{V2T}$ and $\mathbf{F}_{H2V}$ are defined in Appendix B.

$^N \boldsymbol{\omega}^{IN}$ is the angular velocity vector of frame I with respect to frame N (as indicated by the right superscript IN) expressed in frame N (left superscript); we have $^N \boldsymbol{\omega}^{IN} = {}^N \boldsymbol{\omega}^{IE} + {}^N \boldsymbol{\omega}^{EN}$.

$^N \overline{\mathbf{f}}^I$ is estimated specific force expressed in navigation frame.

$[A \times]$ is the skew symmetric matrix of arbitrary vector A.

The discrete-time form of equation (8) is provided in Appendix A. It can be expressed as:

$$\delta \mathbf{x}_{INS, k+1} = \boldsymbol{\Phi}_{INS, k} \delta \mathbf{x}_{INS, k} + \delta \mathbf{w}_{INS, k} \tag{11}$$

where $\boldsymbol{\Phi}_{INS, k}$ is the state transition matrix between time step k and k+1.

2.2 LiDAR Measurement Model

A LiDAR emits laser beams at regular angular intervals and collects light returns after reflection on nearby objects.[13] Signal time to return is used for measuring the distance between the scanner and the objects. LiDAR accuracy depends on its distance to the object, on surface properties of the object and on the angle of incidence of the beam on the target surface. Feature extraction and data association are pre-estimator processes that help exploit raw LiDAR measurements. Feature extraction aims at determining consistently identifiable landmark features (e.g., the axis of a cylinder for a lamp-pole or tree-trunk). Data association assigns the extracted features to the corresponding landmark states. Figure 2 shows a 2D model of a vehicle and a landmarks labeled 'i'. $^i d$ is the range measurement between the LiDAR and landmark i , and $^i \theta$ is the bearing measurement for the same landmark. Let n_L be the number of landmarks in view of the LiDAR: i ranges from 1 to n_L.
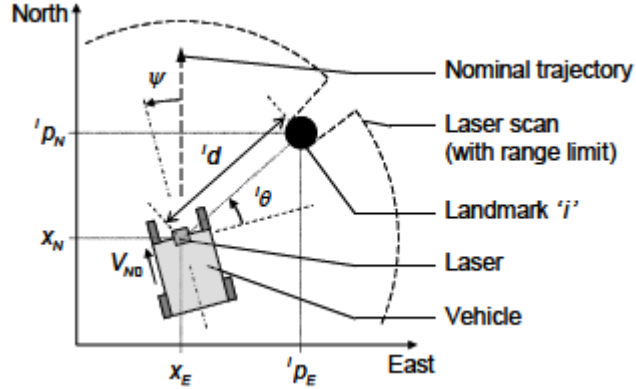
Figure 1. Vehicle and Landmark model

In this work, we only consider the stationary landmarks modeled as vertical cylinders in Section 4, and observed by a two-dimensional LiDAR. Landmark features are the horizontal position coordinates of the cylinder's axis in the navigation frame: ${}^{i}p_E$ and ${}^{i}p_N$ are the east and north positions of landmark i. The 'z' coordinate is not observed. Landmark coordinates are stacked in a landmark state parameter vector, which is constant over time and is expressed as:

$$\mathbf{p} = [{}^{1}p_E \quad {}^{1}p_N \quad \cdots \quad {}^{n_L}p_E \quad {}^{n_L}p_N] \tag{12}$$

$$\mathbf{p}_{k+1} = \mathbf{p}_k \tag{13}$$

Additional parameters in our LiDAR/INS state space realization will include the HAV position $\mathbf{x}$ in navigation frame and its orientation $\mathbf{e}$ (also appearing in equation (8)), which are expressed as:

$$\mathbf{x}_{HAV} = [x_E \quad x_N \quad x_D] \tag{14}$$

$$\mathbf{e}_{HAV} = [\varphi \quad \theta \quad \psi] \tag{15}$$

The non-linear LiDAR ranging and angular measurements are respectively given by:

$$^{i}d = \sqrt{({}^{i}p_E - x_E)^2 + ({}^{i}p_N - x_N)^2} + \upsilon_d \tag{16}$$

$$^{i}\theta = \arctan\left(\frac{{}^{i}p_N - x_N}{{}^{i}p_E - x_E}\right) - \psi + \upsilon_\theta \tag{17}$$

where υ_d and υ_θ are feature measurement errors assumed zero-mean normally distributed.

The nonlinear measurement equation can be written as:

$$\hat{\mathbf{z}}_k = \mathbf{h}_{0,k}(\mathbf{x}_k) + \upsilon_k \tag{18}$$

$$\hat{\mathbf{z}}_k = [d_1 \quad \cdots \quad d_{n_L} \quad \theta_1 \quad \cdots \quad \theta_{n_L}]^T \tag{19}$$

$$\upsilon_k = [\upsilon_{d_1} \quad \cdots \quad \upsilon_{d_{n_L}} \quad \upsilon_{\theta_1} \quad \cdots \quad \upsilon_{\theta_n}]^T \tag{20}$$

where
$\mathbf{x}_k$ is the state vector including HAV position, velocity and orientation states, INS biases, and landmark features.

$\mathbf{v}_k$ is the $2n_L \times 1$ measurement error vector modeled as $\mathbf{v}_k \sim N(\mathbf{0},\ \mathbf{V}_k)$

In equation (18), subscript 0 indicates that state parameters $(^i p_E,\ ^i p_N)$ for the assumed landmark i are correctly matched with their corresponding measurements $(^i d,\ ^i \theta)$. The problem of data association is further described in Section 3.

We can linearize equation (18) using a first-order Taylor series expansion about our best prediction of the vehicle and landmark positions. Stacking the resulting linearized measurements in a ranging vector $\delta\mathbf{d}$, and in an angular measurement vector $\delta\boldsymbol{\theta}$ and also stacking errors in ranging vector error $\mathbf{v}_d$ and in an angular vector error $\mathbf{v}_\theta$, the LiDAR measurement equation can be written as:

$$
\begin{bmatrix} \delta\mathbf{d} \\ \delta\boldsymbol{\theta} \end{bmatrix}_k =
\begin{bmatrix} \mathbf{F}_{d,x} & \mathbf{0} & \mathbf{0} & \mathbf{0} & \mathbf{0} & \mathbf{F}_{d,p} \\ \mathbf{F}_{\theta,x} & \mathbf{0} & -\mathbf{F}_{\theta,e} & \mathbf{0} & \mathbf{0} & \mathbf{F}_{\theta,p} \end{bmatrix}_k
\begin{bmatrix} \delta\mathbf{x}_{HAV} \\ \delta\mathbf{v}_{HAV} \\ \delta\mathbf{e}_{HAV} \\ \delta\mathbf{b}_g \\ \delta\mathbf{b}_a \\ \delta\mathbf{p} \end{bmatrix}_k +
\begin{bmatrix} \mathbf{v}_d \\ \mathbf{v}_\theta \end{bmatrix}_k
\tag{21}
$$

where the coefficient matrices $\mathbf{F}_{d,x}$, $\mathbf{F}_{d,p}$, $\mathbf{F}_{\theta,x}$ and $\mathbf{F}_{\theta,p}$ are defined in Appendix B.

2.3 LiDAR / INS integration

This section describes the integration of INS with LiDAR. The INS state parameters, which include vehicle position, velocity, orientation, accelerometer and gyro biases in equation (11) are augmented with the landmark feature parameters in equation (13), as already shown in equation (21). The state propagation equation for the integrated INS/LiDAR system is:

$$
\begin{bmatrix} \delta\mathbf{x}_{INS} \\ \delta\mathbf{p} \end{bmatrix}_{k+1} =
\begin{bmatrix} \boldsymbol{\Phi}_{INS} & \mathbf{0} \\ \mathbf{0} & \mathbf{I}_{n_L} \end{bmatrix}_k
\begin{bmatrix} \delta\mathbf{x}_{INS} \\ \delta\mathbf{p} \end{bmatrix}_k +
\begin{bmatrix} \delta\mathbf{w}_{INS} \\ \mathbf{0} \end{bmatrix}_k
\tag{22}
$$

Equations (21) and (22) are the integrated LiDAR/INS state space realization.

3. Integrity Risk Evaluation through Correct and Incorrect Data Association

3.1 HAV State Estimation

Assume that we have n_L landmarks and m_F measurements per landmarks (in Figure 1, $m_F = 2$ measurements corresponding to the LiDAR's angular and ranging measurements). In this work, m_F is also the number of features per landmarks ($m_F = 2$ horizontal position coordinates per landmark). The total number of measurements is $n \equiv n_L m_F$. Let $\hat{\mathbf{z}}_k$ be the $n \times 1$ LiDAR measurement vector in (18). We assume that $\hat{\mathbf{z}}_k$ is normally distributed with mean $\mathbf{z}_k$ and covariance matrix $\mathbf{V}_k$. We use the notation: $\hat{\mathbf{z}}_k \sim N(\mathbf{z}_k,\ \mathbf{V}_k)$.

Equation (18) was linearized using the predicted state vector $\bar{\mathbf{x}}_k$. This process can be described using the following equations [22]:

$$
\begin{aligned}
\hat{\mathbf{z}}_k &= \mathbf{h}_{0,k}(\mathbf{x}_k) + \mathbf{h}_{0,k}(\bar{\mathbf{x}}_k) - \mathbf{h}_{0,k}(\bar{\mathbf{x}}_k) + \mathbf{v}_k \\
&\approx \mathbf{h}_{0,k}(\bar{\mathbf{x}}_k) + \mathbf{H}_k(\mathbf{x}_k - \bar{\mathbf{x}}_k) + \mathbf{v}_k
\end{aligned}
\tag{23}
$$

where the observation matrix $\mathbf{H}_k$ is the measurement-to-state coefficient matrix given in equation (21). Using the same notations of equation (23), equation (21) takes the form:

$$\hat{\mathbf{z}}_k - \mathbf{h}_{0,k}(\overline{\mathbf{x}}_k) = \mathbf{H}_k \delta \mathbf{x}_k + \mathbf{v}_k \tag{24}$$

where we defined: $\hat{\mathbf{z}}_k - \mathbf{h}_{0,k}(\overline{\mathbf{x}}_k) \equiv [\delta \mathbf{d}_k^T \quad \delta \boldsymbol{\theta}_k^T]^T$. The state propagation equation (22) is expressed in the form:

$$\delta \mathbf{x}_k = \boldsymbol{\Phi}_{k-1} \delta \mathbf{x}_{k-1} + \delta \mathbf{w}_{k-1} \tag{25}$$

where $\mathbf{w}_k \sim N(\mathbf{0}, \mathbf{W}_k)$.

State prediction and estimation vectors and error covariance matrices are obtained recursively using a Kalman filter:

$$\overline{\mathbf{x}}_k = \boldsymbol{\Phi}_{k-1} \hat{\mathbf{x}}_{k-1} , \quad \overline{\mathbf{P}}_k = \boldsymbol{\Phi}_{k-1} \hat{\mathbf{P}}_{k-1} \boldsymbol{\Phi}_{k-1}^T + \mathbf{W}_{k-1} \tag{26}$$

$$\hat{\mathbf{x}}_k = \overline{\mathbf{x}}_k + \mathbf{K}_k \boldsymbol{\gamma}_{0,k} , \quad \hat{\mathbf{P}}_k = (\mathbf{I} - \mathbf{K}_k \mathbf{H}_k) \overline{\mathbf{P}}_k \tag{27}$$

where $\mathbf{K}_k$ is the Kalman gain defined as $\mathbf{K}_k = \overline{\mathbf{P}}_k \mathbf{H}_k^T (\mathbf{H}_k \overline{\mathbf{P}}_k \mathbf{H}_k^T + \mathbf{V}_k)^{-1}$. $\boldsymbol{\gamma}_{0,k}$ is the innovation vector under correct association, which is given by:

$$\boldsymbol{\gamma}_{0,k} \equiv \hat{\mathbf{z}}_k - \mathbf{h}_{0,k}(\overline{\mathbf{x}}_k) \tag{28}$$

In addition, the state estimation error vector is expressed as:

$$\delta \hat{\mathbf{x}}_k \equiv \hat{\mathbf{x}}_k - \mathbf{x}_k \tag{29}$$

We consider an HAV application where the primary concern is to keep the vehicle inside a lane. Therefore, the positioning error in the direction perpendicular to the lane is of main interest, and is called the hazard state parameter. We can isolate the hazard state parameter estimation error using the following equation:

$$\delta \hat{x}_k \equiv \boldsymbol{\alpha}^T \delta \hat{\mathbf{x}}_k \tag{30}$$

where $\boldsymbol{\alpha}$ is a vector with zeros elements except a one for East direction (in a North-South road). Let σ_k^2 be the variance of the estimation error for the state of interest, then under the correct association hypothesis we can write $\delta \hat{x}_k \sim N(0, \sigma_k^2)$ [24].

3.2 Innovation-Based Data Association

LiDAR measurements $\hat{\mathbf{z}}_k$ are arranged in an arbitrary order at time step k. If n_L landmarks are visible, then there are $(n_L!)$ potential ways for assigning the measurements to landmarks in the EKF, i.e., to state parameters [12]. Incorrect association (IA) happens when the order of measurements is not the same as the assumed order of landmarks in the EKF. We consider all possible orderings of measurements $\overline{\mathbf{z}}_{i,k} = \mathbf{h}_{i,k}(\overline{\mathbf{x}}_k)$ where $i = 0, ..., h$ and $h = n_L! - 1$. Subscript zero is the correct association and all other permutations are incorrect ones.

The innovation vector $\boldsymbol{\gamma}_{i,k}$ will affect the EKF through equation (27). Only in case of correct association is the mean of the innovation vector zero. Any other (incorrect) association causes the mean of the innovation vector to be non-zero. Thus, the innovation vector is a good indicator of incorrect association. The innovation vector can be expressed as [22]:

$$\boldsymbol{\gamma}_{i,k} = \hat{\mathbf{z}}_k - \mathbf{A}_{i,k} \mathbf{h}_{0,k}(\overline{\mathbf{x}}_k) \approx \mathbf{y}_{i,k} + \mathbf{v}_k - \mathbf{A}_{i,k} \mathbf{H}_k \delta \overline{\mathbf{x}}_k \tag{31}$$

where
$$\mathbf{y}_{i,k} \equiv \mathbf{B}_{i,k}\mathbf{h}_{0,k}(\mathbf{x}_k) \quad , \quad \mathbf{y}_{0,k} = \mathbf{0} \tag{32}$$

$$\mathbf{B}_{i,k} \equiv \mathbf{I}_n - \mathbf{A}_{i,k} \quad , \quad \delta\overline{\mathbf{x}}_\mathbf{k} \equiv \overline{\mathbf{x}}_\mathbf{k} - \mathbf{x}_\mathbf{k} \tag{33}$$

and where $\mathbf{A}_{i,k}$ are n×n permutation matrices for $i = 0,...,h$. It is worth noting that the state prediction vector $\overline{\mathbf{x}}_k$ in equations (28) and (31) will be much more accurate using an INS than using a basic HAV kinematic model as in [22]. We will leverage this effect to reduce the risk of incorrect associations in Section 4.

In case of incorrect association, there is a shift $\mathbf{y}_{i,k}$ in the mean of innovation vector. This shift is zero for the correct association hypothesis. The data association criterion is defined as:

$$\min_{i=0,...,h}\left\|\boldsymbol{\gamma}_i\right\|_{\mathbf{Y}_i^{-1}}, \quad \text{where} \quad \mathbf{Y}_i = \mathbf{A}_i\mathbf{H}\overline{\mathbf{P}}\mathbf{H}^\mathrm{T}\mathbf{A}_i^\mathrm{T} + \mathbf{V} \tag{34}$$

3.3 Integrity Risk equation

The integrity risk $P(\mathrm{HMI}_k)$ or probability of hazardous misleading information (HMI) is the probability of the HAV being outside of a specified alert limit box when the vehicle position is estimated to be inside this box. [1-3, 12]. An analytical bound on the integrity risk that considers all possible incorrect associations is expressed as [23]:

$$P(\mathrm{HMI}_k) \le 1 - \left[1 - P(\mathrm{HMI}_k \mid \mathrm{CA}_K)\right]\prod_{j=1}^{k}P(\mathrm{CA}_j \mid \mathrm{CA}_{J-1}) + I_{\mathrm{FE,ALLOC,k}} \tag{35}$$

with
$$P(\mathrm{HMI}_k \mid \mathrm{CA}_K) = Q\left(\ell/\sigma_k\right) + 1 - Q\left(-\ell/\sigma_k\right) \tag{36}$$

$$P(\mathrm{CA}_j \mid \mathrm{CA}_{J-1}) \ge 1 - P\left(q_j^2 \ge \min_{i=1,...,h}\left\{L_{D,j}^2\lambda_{\mathrm{MIN},i,j}^2/4\right\}\right) \tag{37}$$

where
K   designates a range of indices: $K = \{0,...k\}$
$Q(\ )$ is the tail probability function of the standard normal distribution
ℓ is the specified alert limit that defines a hazardous situation
σ_k is the standard deviation of the estimation error for the vehicle state of interest
$I_{\mathrm{REQ,k}}$ is the overall integrity risk requirement
$I_{\mathrm{FE,ALLOC,k}}$ is a predefined integrity risk allocation at FE, chosen to be a small fraction of $I_{\mathrm{REQ,k}}$. [23]
q_j^2 is a chi-square distributed random variable with a number of degrees of freedom that is the sum of the number of measurements and of states at time step j
$L_{D,j}^2$ can be determined at FE, and represents the minimum value of the mean landmark feature separation at time step j. [23]
$\lambda_{\mathrm{MIN},i,j}^2$ can be determined at DA, and is defined to account for the worst-case projection of the FE's separation vector into the DA's innovation space. [23]

4. Covariance analysis and integrity risk evaluation

In this section, we consider the simulation scenario of an HAV roving northwards between two landmarks. We analyze the sensitivity of integrity monitoring performance when using LiDAR only versus using the LiDAR/INS scheme described in Section 2. In particular, we quantify the reduction in risk of incorrect association brought by INS data.

4.1 Traveling through two landmark scenario

Figure 2 represents the two landmarks with black, and the vehicle with black triangle markers. The vehicle starts its trajectory from point (0, 0) and travels 35 meters northwards while passing by the landmarks. LiDAR specifications and other simulation settings can be found in Table. 1.

Table 1 LiDAR Simulation Parameters

System Parameters	Values
Standard deviation on raw laser ranging measurement	0.03 m
Standard deviation on raw laser angular measurement	0.5 deg
Laser range Limit	40 m
Laser data sampling interval	0.5 s
Vehicle speed	1 m/s
Alert limit ℓ	0.45 m
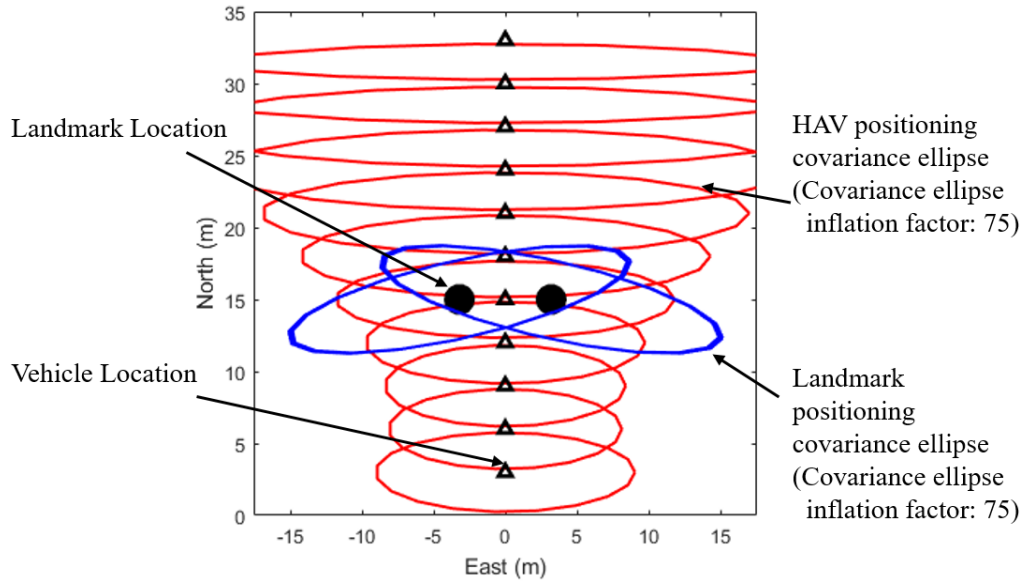
Figure 2. Vehicle and Landmark Positioning Performance using LiDAR-Only

In Figure 2, landmarks are located at (-3.2m, 15m) and (3.2m, 15m). Red covariance ellipses represent the HAV positioning uncertainty and blue ellipses show the landmarks' positioning uncertainty over time. Covariance ellipses are inflated by a factor 75 to facilitate visualization. The positions of the landmarks are initially unknown. In this figure, LiDAR-only is used to simultaneously estimate HAV and landmark positions using a SLAM-like method [5, 22, 24, 25].

In Figure 3, the LiDAR/INS implementation described in Section 2 is evaluated for the same HAV trajectory and landmark geometry as in Figure 2 (landmark separation distance of 6.4 meters). Table 2 describes the INS parameter values used in this simulation. In Figure 3, red and blue ellipses represent LiDAR/INS positioning errors for the HAV and landmarks, respectively. As expected, the ellipses in this figure are smaller than in Figure 2, because adding INS to LiDAR improves both the HAV and landmark position estimation performance.
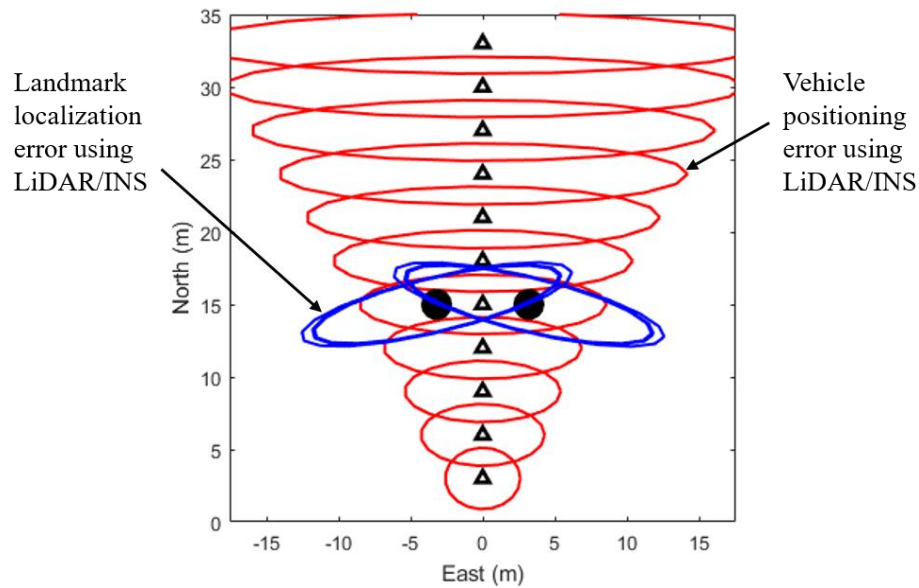
Figure 3. Positioning Error Covariance Ellipses Using the Proposed LiDAR/INS Implementation

Table 2. INS Simulation Parameters

System Parameters	Values
Accelerometr velocity random walk	$0.022 \ \text{m/s}^2/\sqrt{\text{Hz}}$
Gyroscope angle random walk	$0.15 \ \ \text{deg}/\sqrt{\text{hr}}$
Accelerometer time constant	3600 s
Gyroscope time constant	3600 s
Standard deviation of accelerometer GMRP bias	$0.1 \ \text{m/s}^2$
Standard deviation of Gyroscope GMRP bias	$0.2 \ \ \text{deg}$

Figure 4 shows the contribution of INS in reducing the standard deviation of the HAV lateral positioning error. The red line is the standard deviation of the LiDAR/INS lateral positioning error over time (which is also represented in Figure 3 as the horizontal semi-major axis of the red ellipses). The red LiDAR/INS curve in Figure 4 is lower than the black LiDAR-Only curve. As expected, INS data help reduce the positioning error standard deviation, noted σ_k in equation (36). σ_k impacts the $P(\text{HMI}_k|\text{CA}_K)$-term in the $P(\text{HMI}_k)$-equation (35), and this is the first process through which the INS contributes to integrity risk reduction.
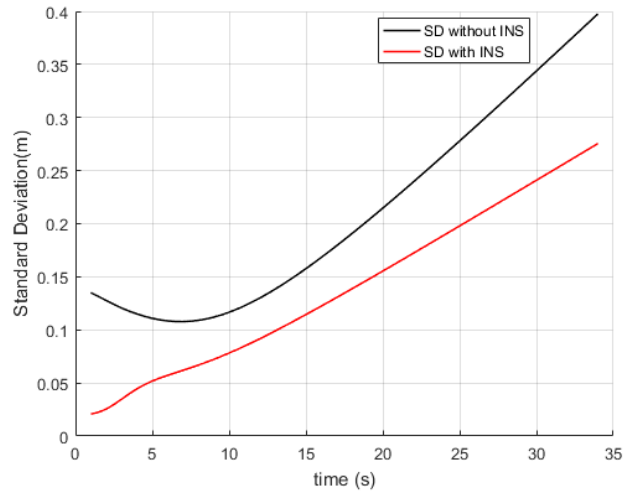
Figure 4. HAV Lateral Positioning Error Standard Deviations for Lidar-Only and LiDAR/INS

In parallel, Figure 5 shows bounds on the probability incorrect association for LiDAR-Only in black, and for LiDAR/INS in red. The risk of incorrect association can be expressed as: $P(IA_K) = 1 - P(CA_K)$, where the probability of correct association ($P(CA_K) = \prod_{j=1}^{k} P(CA_j | CA_{J-1})$) is expressed in equation (35). This figure shows the contribution of the INS to reducing the risk of LiDAR incorrect association, thereby reducing the $P(HMI_k)$-bound in equation (35).
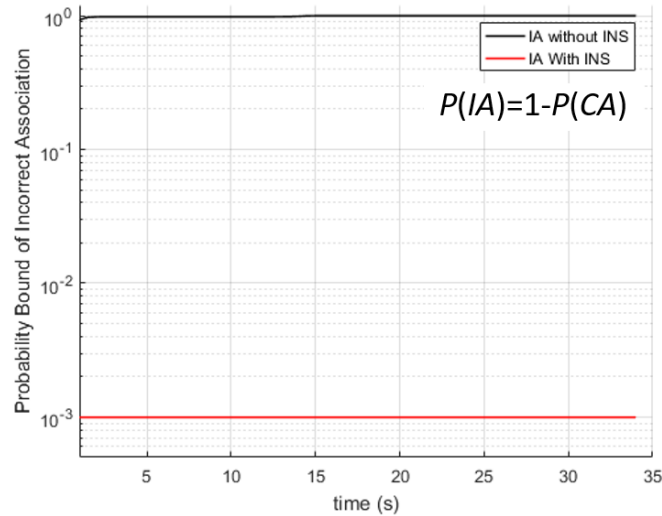

Figure 5. Probability of Incorrect Data Association

Figure 6 shows the integrity risk curves assuming CA and accounting for potential incorrect associations. The dashed curves represent the $P(HMI_k | CA_K)$ directly derived from the EKF variance in equation (36), and the solid lines represent the total $P(HMI_k)$ accounting for potential incorrect associations for LiDAR-Only (in black) and for LiDAR/INS (in red). The solid lines are orders of magnitude higher than the dashed lines, which illustrates the significant impact of the risk of incorrect association on $P(HMI_k)$. In addition, the solid red line is two to three orders of magnitude lower than the solid black line, showing a significant overall risk reduction using LiDAR/INS as compared to LiDAR-Only.
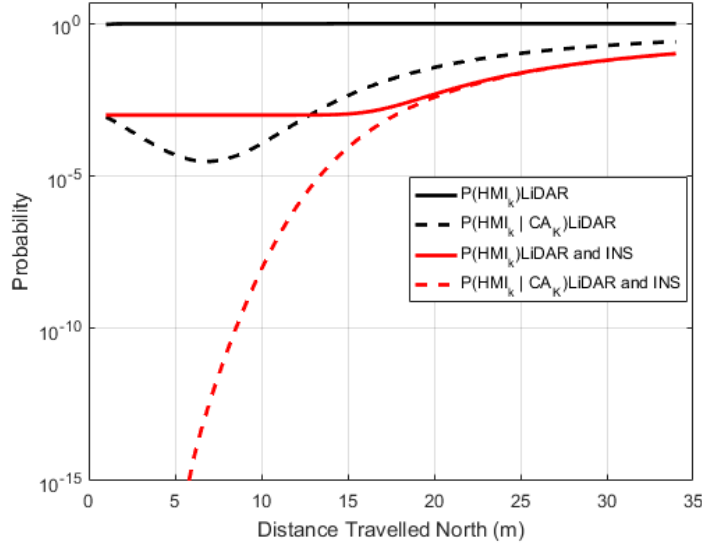
Figure 6. Integrity Risk Bounds Assuming Correct Associations (dashed) Versus Accounting for Incorrect Associations (solid), For LiDAR-Only (black) Versus LiDAR/INS (red).

5. Conclusion

This paper describes a LiDAR/INS integration method that enables integrity risk evaluation. We implemented a Kalman filter innovation-based risk evaluation method to account for all possible incorrect associations affecting LiDAR-based navigation. Performance evaluations showed that landmarks located at close distance from each other could cause significant risk of incorrect association. For an example scenario, we quantified the reduction in incorrect association risk and integrity risk provided by our LiDAR/INS integration scheme as compared to a LiDAR-only implementation.

Appendix A

This appendix describes discrete-time, linearized equations for vehicle dynamics and INS errors.

Nonlinear Vehicle Dynamics Equations:

The continuous, nonlinear equations for the HAV velocity vector $\mathbf{v}_{HAV}(t)$ and position vector $\mathbf{x}_{HAV}(t)$ can be written as [19, 20]:

$$ {}^{N}\mathbf{v}_{HAV}^{E}(t) = \int_{0}^{t} {}^{N}\mathbf{f}^{I}\, dt - \int_{0}^{t} (2\,{}^{N}\boldsymbol{\omega}^{IE} + {}^{N}\boldsymbol{\omega}^{EN}) \times {}^{N}\mathbf{v}_{HAV}^{E}\, dt + \int_{0}^{t} {}^{N}\mathbf{g}^{E}\, dt \tag{A.1} $$

$$ {}^{N}\mathbf{x}_{HAV}^{E}(t) = \int_{0}^{t} {}^{N}\mathbf{v}_{HAV}^{E}\, dt \tag{A.2} $$

In the following equations, we determine the discrete-time time-propagation of the rotation matrix between body and navigation frames (We describe this rotation matrix because the INS measurements are provided in body frame):

$$ \dot{\mathbf{C}}_{B}^{N} = \mathbf{C}_{B}^{N}[{}^{B}\overline{\boldsymbol{\omega}}^{IB}\times] \tag{A.3} $$

where
$\mathbf{C}_{B}^{N}$ is the transformation matrix from body to navigation frame [19]
$[{}^{B}\overline{\boldsymbol{\omega}}^{IB}\times]$ is the skew symmetric matrix of the estimated angular velocity vector of frame B w.r.t frame I expressed in B

In discrete-time form between time steps t_k and t_{k+1}, equation (A.3) becomes [19]:

$$\mathbf{C}_{B,k+1}^{N} = \mathbf{C}_{B,k}^{N} e^{\int_{t_k}^{t_{k+1}} [\,^{B}\overline{\boldsymbol{\omega}}^{IB} \times]dt} \tag{A.4}$$

Also, we define the vector of angular variation from t_k to t_{k+1} as:

$$\boldsymbol{\alpha}_{k+1} = \int_{t_k}^{t_{k+1}} {}^{B}\overline{\boldsymbol{\omega}}^{IB} dt \approx {}^{B}\overline{\boldsymbol{\omega}}^{IB} T_S, \quad \text{where} \quad T_S = t_{k+1} - t_k \tag{A.5}$$

Thus, we can rewrite equation (A.4) as follows:

$$\mathbf{C}_{B,k+1}^{N} = \mathbf{C}_{B,k}^{N} e^{[\boldsymbol{\alpha}_{k+1} \times]} = \mathbf{C}_{B,k}^{N} \mathbf{A}_k \tag{A.6}$$

where $[\boldsymbol{\alpha}_{k+1} \times]$ is the skew symmetric matrix for vector $\boldsymbol{\alpha}_{k+1}$, and where $\mathbf{A}_k$ is defined as:

$$\mathbf{A}_k = \mathbf{I} + \frac{\sin|\boldsymbol{\alpha}_{k+1}|}{|\boldsymbol{\alpha}_{k+1}|}[\boldsymbol{\alpha}_{k+1} \times] + \frac{1 - \cos|\boldsymbol{\alpha}_{k+1}|}{|\boldsymbol{\alpha}_{k+1}|^2}[\boldsymbol{\alpha}_{k+1} \times] \tag{A.7}$$

Next, we write the discrete-time form of the first term in equation (A.1), which is the integral of the specific force with respect to inertial frame. $\mathbf{u}_k^E$ is the change in vehicle velocity with respect to the earth from t_k to t_{k+1}, and it is expressed as:

$$^{N}\mathbf{u}_k^{E} = \int_{t_k}^{t_{k+1}} {}^{N}\overline{\mathbf{f}}^{I} dt \tag{A.8}$$

where $^{N}\mathbf{u}_k^{E}$ is the change in vehicle velocity from t_k to t_{k+1} expressed in navigation frame. In practice, the specific force is measured by the INS in the body frame. We can use equations (A.6) and (A.8) to transform the specific force vector from body frame to navigation frame.

$$^{N}\mathbf{u}_k^{E} \approx \mathbf{C}_{B,k}^{N} \mathbf{A}_k {}^{B}\overline{\mathbf{f}}^{I} T_S \tag{A.9}$$

For small angular variations, we can approximate equation (A.7) as [19]:

$$\mathbf{A}_k \approx \mathbf{I} + [\boldsymbol{\alpha}_{k+1} \times] \tag{A.10}$$

Substituting equation (A.10) in equation (A.9), we obtain the following equation:

$$^{B}\mathbf{u}_k^{E} = \mathbf{C}_k^{NB} \left[\int_{t_k}^{t_{k+1}} {}^{B}\overline{\mathbf{f}}^{I} dt + \int_{t_k}^{t_{k+1}} \boldsymbol{\alpha}_{k+1} \times {}^{B}\overline{\mathbf{f}}^{I} dt \right] \tag{A.11}$$

We then define the following vector:

$$\mathbf{v}_{k+1}^{*} = \int_{t_k}^{t_{k+1}} {}^{B}\overline{\mathbf{f}}^{I} dt \tag{A.12}$$

By integrating the cross product in equation (A.11) by parts, we can find the following equation [19]:

$$^{N}\mathbf{u}_k^{E} = \mathbf{C}_{B,k}^{N} \left[\mathbf{v}_{k+1}^{*} + 0.5\boldsymbol{\alpha}_{k+1} \times \mathbf{v}_{k+1}^{*} + 0.5 \int_{t_k}^{t_{k+1}} \left(\boldsymbol{\alpha}_{k+1} \times {}^{B}\overline{\mathbf{f}}^{I} - {}^{B}\overline{\boldsymbol{\omega}}^{IB} \times \mathbf{v}_{k+1}^{*} \right) dt \right] \tag{A.13}$$

If $^B\overline{\boldsymbol{\omega}}^{IB}$ and $^B\overline{\mathbf{f}}^I$ remain constant over the update interval, then the integral term in equation (A.13) cancels out. By substituting equation (A.13) in (A.1) and making a small time-interval assumption for the terms, we can write the discrete-time form of the vehicle velocity and position equations as:

$$^N\mathbf{v}^E_{HAV,k+1} = {}^N\mathbf{v}^E_k + {}^N\mathbf{u}^E_k - \left(2[{}^N\boldsymbol{\omega}^{IE}_k\times]T_S + [{}^N\boldsymbol{\omega}^{EN}_k\times]T_S\right)\times {}^N\mathbf{v}^E_{HAV,k} + {}^N\mathbf{g}^E T_S \tag{A.14}$$

$$^N\mathbf{x}^E_{HAV,K+1} = \mathbf{x}_k + \left(\frac{{}^N\mathbf{v}^E_{HAV,k} + {}^N\mathbf{v}^E_{HAV,k+1}}{2}\right)T_S \tag{A.15}$$

where
k   is an index identifying the time step
T_S is time step between iterations k and k+1

Equation (A.15) uses a trapezoidal method as an example numerical integration to determine vehicle displacement. Other integration methods (e.g., such as Simpson's rule or a Runge Kutta fourth order method) can be used as alternatives.

INS error equation:

We can use the Van Loan algorithm to determine the discrete-time state propagation matrix $\boldsymbol{\Phi}_{INS,k}$ based on the continuous-time matrices $\mathbf{F}_{INS,}$ and $\delta\mathbf{w}_{INS}$ [20]. The following equations are the discrete-time form of equations (2, 3, 5, 6)

$$^B\tilde{\mathbf{f}}^I_k = [\mathbf{I}+\mathbf{S}_{a,SF}+\mathbf{M}_{a,MIS}]\,{}^B\mathbf{f}^I_k + \mathbf{b}_{a0} + \mathbf{b}_{a,k} + \boldsymbol{\upsilon}_{a,k} \tag{A.16}$$

$$^B\overline{\mathbf{f}}^I_k = [\mathbf{I}+\hat{\mathbf{S}}_{a,SF}+\hat{\mathbf{M}}_{a,MIS}]^{-1}({}^B\tilde{\mathbf{f}}^I_k - \hat{\mathbf{b}}_{a0}) \tag{A.17}$$

$$^B\tilde{\boldsymbol{\omega}}^{IB}_k = [\mathbf{I}+\mathbf{S}_{g,SF}+\mathbf{M}_{g,MIS}]\,{}^B\boldsymbol{\omega}^{IB}_k + \mathbf{b}_{g0} + \mathbf{b}_{g,k} + \boldsymbol{\upsilon}_{g,k} \tag{A.18}$$

$$^B\overline{\boldsymbol{\omega}}^{IB}_k = [\mathbf{I}+\hat{\mathbf{S}}_{g,SF}+\hat{\mathbf{M}}_{g,MIS}]^{-1}({}^B\tilde{\boldsymbol{\omega}}^{IB}_k - \hat{\mathbf{b}}_{g0}) \tag{A.29}$$

The following equations are the discrete-time form of equations (4) and (7)

$$\mathbf{b}_{a,k+1} = e^{-\frac{T_S}{\tau_a}}\mathbf{b}_{a,k} + \mathbf{n}_{a,k} \tag{A.20}$$

$$\mathbf{b}_{g,k+1} = e^{-\frac{T_S}{\tau_g}}\mathbf{b}_{g,k} + \mathbf{n}_{a,k} \tag{A.21}$$

Appendix B

In this appendix, we describe the coefficient matrices used in equations (10) and (27). The coefficient matrices used in equation (10) are [19]:

$$\mathbf{F}_{V2T} = \begin{bmatrix} 0 & \dfrac{1}{R+h} & 0 \\[2mm] \dfrac{1}{R+h} & 0 & 0 \\[2mm] 0 & \dfrac{-\tan(\lambda)}{R+h} & 0 \end{bmatrix} \tag{B.1}$$

$$\mathbf{F}_{H2V} = \begin{bmatrix} 0 & -\dfrac{2g_0}{R} & 0 \\ \dfrac{2g_0}{R} & 0 & 0 \\ 0 & 0 & 0 \end{bmatrix} \tag{B.2}$$

where
R is the earth radius
h is the vehicle altitude
λ is the vehicle latitude
g_0 is the acceleration of gravity at zero altitude

The coefficients matrices in equations (21) are [4]:

$$\mathbf{F}_{d,x} = \begin{bmatrix} -\dfrac{{}^{1}p_E - x_E}{\left\| {}^{1}\mathbf{p} - \mathbf{x}_{EN} \right\|} & \cdots & -\dfrac{{}^{n_L}p_E - x_E}{\left\| {}^{n_L}\mathbf{p} - \mathbf{x}_{EN} \right\|} \\ -\dfrac{{}^{1}p_N - x_N}{\left\| {}^{1}\mathbf{p} - \mathbf{x}_{EN} \right\|} & \cdots & -\dfrac{{}^{n_L}p_N - x_N}{\left\| {}^{n_L}\mathbf{p} - \mathbf{x}_{EN} \right\|} \end{bmatrix}^{T} \tag{B.3}$$

$$\mathbf{F}_{d,p} = \begin{bmatrix} \dfrac{{}^{1}p_E - x_E}{\left\| {}^{1}\mathbf{p} - \mathbf{x}_{EN} \right\|} & \dfrac{{}^{1}p_N - x_N}{\left\| {}^{1}\mathbf{p} - \mathbf{x}_{EN} \right\|} & 0 & 0 & 0 & 0 \\ 0 & 0 & \ddots & \ddots & 0 & 0 \\ 0 & 0 & 0 & 0 & \dfrac{{}^{n_L}p_E - x_E}{\left\| {}^{n_L}\mathbf{p} - \mathbf{x}_{EN} \right\|} & \dfrac{{}^{n_L}p_N - x_N}{\left\| {}^{n_L}\mathbf{p} - \mathbf{x}_{EN} \right\|} \end{bmatrix} \tag{B.4}$$

$$\mathbf{F}_{\theta,x} = \begin{bmatrix} \dfrac{{}^{1}p_N - x_N}{\left\| {}^{1}\mathbf{p} - \mathbf{x}_{EN} \right\|^{2}} & \cdots & \dfrac{{}^{n_L}p_N - x_N}{\left\| {}^{n_L}\mathbf{p} - \mathbf{x}_{EN} \right\|^{2}} \\ -\dfrac{{}^{1}p_E - x_E}{\left\| {}^{1}\mathbf{p} - \mathbf{x}_{EN} \right\|^{2}} & \cdots & -\dfrac{{}^{n_L}p_E - x_E}{\left\| {}^{n_L}\mathbf{p} - \mathbf{x}_{EN} \right\|^{2}} \end{bmatrix}^{T} \tag{B.5}$$

$$\mathbf{F}_{\theta,x} = \begin{bmatrix} -\dfrac{{}^{1}p_N - x_N}{\left\| {}^{1}\mathbf{p} - \mathbf{x}_{EN} \right\|^{2}} & \dfrac{{}^{1}p_E - x_E}{\left\| {}^{1}\mathbf{p} - \mathbf{x}_{EN} \right\|^{2}} & 0 & 0 & 0 & 0 \\ 0 & 0 & \ddots & \ddots & 0 & 0 \\ 0 & 0 & 0 & 0 & -\dfrac{{}^{n_L}p_N - x_N}{\left\| {}^{n_L}\mathbf{p} - \mathbf{x}_{EN} \right\|^{2}} & \dfrac{{}^{n_L}p_E - x_E}{\left\| {}^{n_L}\mathbf{p} - \mathbf{x}_{EN} \right\|^{2}} \end{bmatrix} \tag{B.6}$$

$$\mathbf{F}_{\theta,p} = \begin{bmatrix} 0 & 0 & 0 \\ 0 & 0 & 0 \\ 0 & 0 & 1 \\ & \vdots & \\ 0 & 0 & 0 \\ 0 & 0 & 0 \\ 0 & 0 & 1 \end{bmatrix}_{3n_L x 3} \tag{B.7}$$

ACKNOWLEDGMENTS

References

[1] DeCleene, B. "Defining Pseudorange Integrity – Overbounding," *Proc. ION GPS 2000, Salt Lake City, UT., 2000,* pp. 1916-1924.

[2] Rife, J., Pullen, S., Enge, P. and Pervan, B. "Paired Overbounding for Nonideal LAAS and WAAS Error Distributions." *IEEE TAES,* Vol. 42, No. 4, 2006 pp. 1386-1395.

[3] Joerger, M., and B. Pervan. "Measurement-Level Integration of Carrier-Phase GPS and Laser-Scanner for Outdoor Ground Vehicle Navigation." *ASME Journal of Dynamic Systems, Measurement, and Control. 131. 2009.*

[4] Joerger, M. "Carrier Phase GPS Augmentation Using Laser Scanners and Using Low Earth Orbiting Satellites," *Ph.D. Dissertation*, Illinois Institute of Technology, 2009.

[5] Bailey, T. "Mobile Robot Localisation and Mapping in Extensive Outdoor Environments," *PhD Dissertation*, The University of Sydney, 2002.

[6] Cooper, A.J. "A Comparison of Data Association Techniques for Simultaneous Localization and Mapping," *M.S. Thesis*, Massachussetts Institute of Technology, 2005.

[7] Tena Ruiz, I., Petillot, Y., Lane, D. M. and Salson, C. "Feature Extraction and Data Association for AUV Concurrent Mapping and Localisation," *Proc. IEEE-ICRA, 2001.*

[8] Nguyen, V., Martinelli, A., Tomatis, N., and Siegwart, R. "A Comparison of Line Extraction Algorithms using 2D Laser Rangefinder for Indoor Mobile Robotics," *Proc. IEEE/RSJ IROS, 2005.*

[9] Bar-Shalom, Y. and Fortmann, T. E. "Tracking and Data Association," *Mathematics in Science and Engineering*, Vol. 179, Academic Press, 1988.

[10] Pfister, S. T., Kriechbaum, K. L., Roumeliotis, S. I., Burdick, J. W. "Weighted Range Sensor Matching Algorithms for Mobile Robot Displacement Estimation," *Proc IEEE ICRA*, *2002.*

[11] Thrun, S., Burgard, W. and Fox, D. "A Probabilistic Approach to Concurrent Mapping and Localization for Mobile Robots," *Machine Learning and Autonomous Robots*, Vol. 31, No. 5, 1998, pp. 1-25.

[12] Joerger, M., Jamoom, M., Spenko, M. and Pervan, B. "Integrity of Laser-Based Feature Extraction and Data Association," *Proceedings of IEEE/ION PLANS 2016, Savannah, GA, April 2016*, pp. 557-571.

[13] Joerger, M., Pervan, B. "Continuity Risk of Feature Extraction for Laser-Based Navigation," *Proceedings of the 2017 International Technical Meeting of The Institute of Navigation, Monterey, California, January 2017*, pp. 839-855.

[14] Joerger, M., Arana Duenas, G., Spenko, M. and Pervan, B. "Landmark Data Selection and Unmapped Obstacle Detection in Lidar-Based Navigation," *Proceedings of the 30th International Technical Meeting of The Satellite Division of the Institute of Navigation (ION GNSS+ 2017), Portland, Oregon, September 2017*, pp. 1886-1903.

[15] Duenas Arana, G., Joerger, M., and Spenko, M. "Minimizing Integrity Risk via Landmark Selection in Mobile Robot Localization." accepted for publication in *Proceedings of IEEE International Conference on Robotics and Automation (ICRA2018). Brisbane, Australia. 2018.*

[16] Opromolla, R., Fasano, G., Rufino, G., Grassi, M. and Savvaris, A. " LIDAR-Inertial Integration for UAV Localization and Mapping in Complex Environment." *International Conference on Unmanned Aircraft Systems (ICUAS), 2016*

[17] Soloviev, A., Bates, D. and Van Graas. F. " Tight Coupling of Laser Scanner and Inertial Measuring for Fully Autonomous Relative Navigation Solution." *Navigation*, 54(3), pp.189-205, 2007

[18] Soloviev. A. " Tight Coupling of GPS, Laser Scanner and Inertial Measuring for Navigation in Urban Environment." *IEEE/ION Position, Location and Navigation Symposium, 2008*

[19] Titterton, D., Weston, J. "Strapdown inertial navigation technology." Stevenage: The Inst. of Engineering and Technology, 2009

[20] Rogers, R. "Applied mathematics in integrated navigation systems." 3rd ed. Reston: American Institute of Aeronautics and Astronautics, 2007

[21] Brown, R. Hwang, P. "Introduction to Random Signals and Applied Kalman Filtering. Hoboken." NJ: John Wiley and Sons, 2012

[22] Williams, S.B., Dissanayake, G. and Durrant-Whyte, H. "An efficient Approach to the Simultaneous Localisation and Mapping Problem," *Proc. IEEE-ICRA, 2002*

[23] Joerger, M. Pervan, B. "Quantifying Safety of Laser-Based Navigation," in press. *IEEE Transactions on Aerospace and Electronic Systems, 2018*

[24] Thrun, S. "Robotic Mapping: A Survey," *Exploring Artificial Intelligence in the New Millenium, G. Lakemeyer and B. Nebel. 2002*

[25] Leonard, J., Durrant-Whyte, H. "Directed Sonar Sensing for Mobile Robot Navigation," *Kluwer Academic Publishers*, Cambridge, MA, 1992, pp. 129-138.